

# The Martensitic Transformation and Strain-Hardening Behavior of Austenitic Steels During Fatigue and Tensile Loading

G.R. LEHNHOFF<sup>1</sup> and K.O. FINDLEY<sup>1,2</sup>

1.—Department of Metallurgical and Materials Engineering, Colorado School of Mines, 1500 Illinois St., Golden, CO 80401, USA. 2.—e-mail: kfindley@mines.edu

The tensile and low-cycle fatigue deformation and  $\alpha'$ -martensitic transformation behavior of three austenitic steels with varied silicon, aluminum, and nickel levels were characterized using mechanical testing and transmission electron microscopy. Silicon alloying promoted deformation twinning and high work-hardening rates in tension by lowering the stacking fault energy (SFE). Deformation twins and their intersections served as martensite nucleation sites in tension. Martensitic transformation was maximized in the alloy with a low SFE, which increased the alloy capacity to form strain-induced nucleation sites, and low nickel content, which increased the thermodynamic driving force for martensite formation. In fatigue loading, martensite nucleation occurred on localized austenite shear bands composed of dissociated dislocations that form in the cyclically stabilized portion of the fatigue life. The shear bands occurred in all materials irrespective of the SFE. The extent of martensitic transformation in fatigue is apparently dictated more by thermodynamic driving force for transformation and not by SFE. In both tension and fatigue, martensite formation led to strain hardening.

## INTRODUCTION

Enhanced strength and ductility can be obtained in steel alloys through deformation-induced transformation of austenite to martensite. This phenomenon occurs in many alloy systems including stainless steels, multiphase transformation-induced plasticity steels, and quenched and partitioned steels, among others. The current study focuses on strain-induced martensitic transformation, which occurs as martensite nucleates at shear band intersections during monotonic loading.<sup>1,2</sup> Deformation-induced martensite has been reported to form on shear bands and shear band intersections during fatigue loading.<sup>3–7</sup>

Although it is well understood that factors such as austenite stacking fault energy (SFE) and thermodynamic driving force for austenite-to-martensite transformation are especially important parameters related to austenite stability during monotonic loading,<sup>1</sup> there is a lack of fundamental understanding of how some of these same factors affect its stability during cyclic loading. Furthermore, fatigue loading introduces additional time- and cycle-dependent factors such as the accumulation of

plastic strain and evolution of dislocation substructure that may also influence austenite stability.

This study uses three metastable austenitic steels to compare strain-induced martensite formation in tension and fatigue. The effect of martensite formation and deformation twinning on strain-hardening behavior during tension and fatigue is also presented.

## EXPERIMENTAL DETAILS

The compositions, annealing temperatures, and grain sizes of the three steels are shown in Table I.

The alloy design strategy was based on a study of the Fe-Ni-Cr-Si-Al system that had the objective of identifying combinations of ferrite stabilizing elements (Cr, Si, and Al) and Ni, an austenite stabilizing element, that yield fully austenitic steels.<sup>8</sup> The differences in Ni, Al, and Si contents among the three alloys alter the SFE and thermodynamics of the austenite-to- $\alpha'$ -martensite phase transformation. The SFE was measured through partial dislocation spacing measurements.<sup>9</sup> The SFE of the 2.5 Al alloy was measured to be  $38.3 \text{ mJ/m}^2 \pm 6.1 \text{ mJ/m}^2$ , and the SFE of the 2.5 Si alloy was measured to be

**Table I. Experimental steel compositions, annealing temperatures, and grain sizes**

wt.%	C	N	Ni	Cr	Mn	Si	Al	Annealing temperature (°C)	Grain size ( $\mu\text{m}$ )
2.5 Al	0.030	0.0034	15.04	11.02	1.08	0.034	2.47	1060	126 $\pm$ 5
2.5 Si	0.028	0.0036	14.99	10.98	1.10	2.50	0.06	1075	138 $\pm$ 5
2.8 Si:L-Ni	0.016	0.016	13.46	10.74	0.97	2.85	0.07	1100	157 $\pm$ 5

19.9  $\text{mJ/m}^2 \pm 2.0 \text{ mJ/m}^2$ .<sup>9</sup> Although the SFE of the 2.8 Si:L-Ni alloy was not measured, it is speculated to be closer to that of the 2.5 Si alloy because of the similarity in Si and Al alloying; this assertion is supported by experimental data presented later. The alloys were cast, homogenized for 20 h at 1200°C, and then annealed at the temperatures shown in Table I.

Round bar specimens with a gage diameter of 6.4 mm and gage length of 19 mm were used for tensile and low-cycle fatigue (LCF) testing following the guidelines in ASTM E606.<sup>10</sup> Mechanical testing was performed on an MTS servo-hydraulic frame (MTS Systems Corporation, Eden Prairie, MN). Tensile tests were performed at an actuator displacement rate of 5.1 mm/min. Two tensile specimens per alloy were tested to failure to obtain tensile properties, whereas one test per alloy was interrupted periodically to measure the martensite content with a Feritscope (Thermo Fischer Scientific Inc., Waltham, MA), which outputs a magnetic fraction of the specimen. The magnetic fraction is related to the fraction of  $\alpha'$ -martensite in a sample because  $\alpha'$ -martensite is ferromagnetic, whereas the austenite is paramagnetic. Talonen et al.<sup>11</sup> reported that the magnetic fractions measured with a Feritscope on flat sheet samples should be multiplied by 1.7 to obtain martensite fractions because the Feritscope is calibrated for ferrite instead of martensite. It has also been shown that the measurements taken on the curved surfaces of round bar samples differ from those taken on flat surfaces.<sup>9</sup> In this article, the data are simply reported as the measured Feritscope magnetic fractions without any assumptions about correction factors for specimen geometry or martensite versus ferrite.

Fully reversed axial LCF tests were performed at 0.6% total strain amplitude and a frequency of 1 Hz with a sinusoidal waveform. One test per alloy was performed until failure to ascertain the cyclic hardening response. Companion specimens were cycled to various fractions of the fatigue life to characterize the martensite content as a function of the cycle number with the Feritscope and to perform transmission electron microscopy (TEM).

A Phillips CM12 TEM (Phillips, Amsterdam, The Netherlands) was used to evaluate the deformation mechanisms of the experimental alloys. Diffraction rotation was corrected using elongated crystals of  $\text{MoO}_3$ .<sup>12,13</sup> Slices of the deformed experimental alloys were sectioned at 45° to the loading axis, ground to a thickness of approximately 140  $\mu\text{m}$  with

a 600-grit surface finish, punched into 3-mm disks, and then twin jet electropolished at approximately 30 mA and 25 V to 50 V in a 95% acetic acid and 5% perchloric acid electrolyte at room temperature.

## RESULTS AND DISCUSSION

### Tensile Deformation Behavior

Figure 1a shows the tensile true stress versus strain and strain-hardening rate versus strain data for the experimental alloys. The strain-hardening rate of the 2.5 Al alloy continuously decreases with increasing true strain up to the point of tensile instability. In contrast, the 2.5 Si alloy demonstrates a plateau in the strain-hardening rate between 0.1 and 0.3 true strain, followed by a continuous decrease in work-hardening rate up to the point of tensile instability. The 2.8 Si:L-Ni alloy displays similar work-hardening behavior to the 2.5 Si alloy, except that higher strain-hardening rates are achieved in the 2.8 Si:L-Ni alloy at true strains above 0.1. Higher work-hardening rates in the 2.8 Si:L-Ni alloy lead to higher strength and ductility relative to the other two alloys; the tensile properties of all three alloys are summarized in Table II.

Figure 1b shows the evolution of magnetic ( $\alpha'$ -martensite) fraction with applied true strain for the three alloys. The open symbol data correspond to Feritscope readings taken during interrupted tensile tests of a single specimen for each material. The closed symbols correspond to measurements taken after failure from two uninterrupted tensile specimens for each material. The largest amount of austenite-to-martensite transformation occurred in the 2.8 Si:L-Ni alloy, followed by the 2.5 Al alloy. A minimal amount of austenite-to-martensite transformation occurred in the 2.5 Si alloy. The large amount of deformation-induced martensite in the 2.8 Si:L-Ni alloy is expected to contribute to the high work-hardening capacity of this alloy. However, martensite formation alone does not explain the trends in work-hardening behavior. The 2.5 Si alloy demonstrates higher work-hardening rates than the 2.5 Al alloy even though the 2.5 Al alloy undergoes more deformation-induced martensitic transformation than the 2.5 Si alloy (Fig. 1b). TEM was used to evaluate the tensile work-hardening mechanisms of the three alloys.

Figure 2a shows a bright-field (BF) TEM micrograph of martensite formation on twin intersections

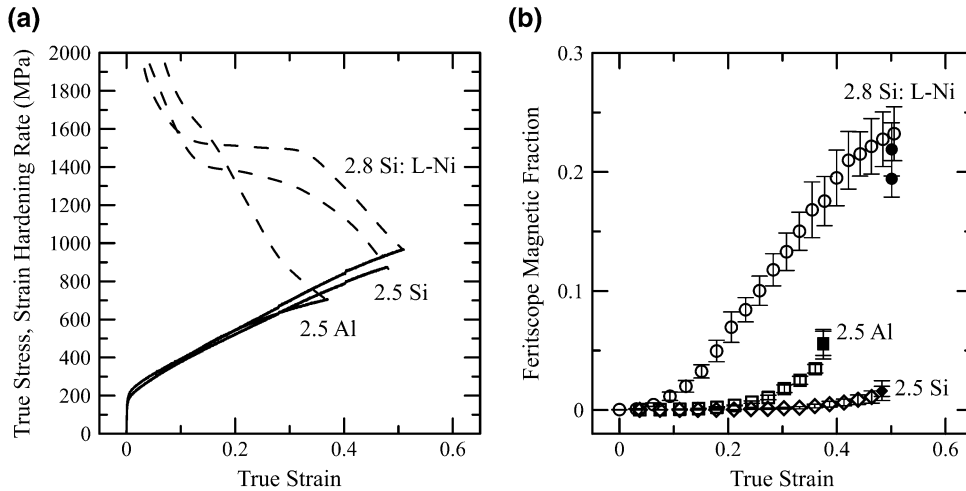


Fig. 1. (a) True stress versus strain (solid lines) and strain-hardening rate versus strain (dashed lines) data for the three alloys. (b) Evolution of magnetic fraction with applied true strain for the three alloys. Open symbols indicate the measurements taken from interrupted tests; closed symbols indicate the measurements taken after failure in tests conducted without interruption.

**Table II. Summary of tensile stress-strain properties**

Material	Engineering				True	
	YS (0.2%) (MPa)	UTS (MPa)	Uniform elongation	Total elongation	UTS (MPa)	Uniform elongation
2.5 Al	167	489	0.45	0.93	709	0.37
2.5 Si	177	540	0.62	1.06	875	0.48
2.8 Si:L-Ni	193	580	0.65	1.05	957	0.50

UTS ultimate tensile strength, YS yield strength.

in the 2.5 Si alloy at 0.48 true strain. Although martensite formation was relatively scarce in the 2.5 Si alloy (Fig. 1b), twin intersections served as nucleation sites for a small amount of martensite particles, as shown in Fig. 2a. Figure 2b shows the corresponding selected-area diffraction pattern (SADP) and schematic representations of the martensite and the two deformation twin diffraction patterns relative to the parent austenite diffraction pattern. The deformed microstructure of the 2.5 Si alloy was dominated by primary and secondary deformation twinning.

Figure 3a shows a dark-field (DF) TEM micrograph of martensite in the 2.8 Si:L-Ni alloy at 0.5 true strain. Pronounced deformation twinning also occurred in the 2.8 Si:L-Ni alloy, similar to that which was observed in the 2.5 Si alloy. Figure 3b shows a BF TEM micrograph of primary deformation twinning in the 2.8 Si:L-Ni alloy at 0.14 true strain. A lower true strain of 0.14 was chosen to observe primary twinning in the 2.8 Si:L-Ni alloy because the extensive martensite formation at larger strains impeded twin identification via TEM.

Figure 4a shows a BF TEM micrograph of primary deformation twins interspersed with small martensite particles in the 2.5 Al alloy at 0.37 true strain. The martensite particles are indicated in the

DF TEM micrograph shown in Fig. 4b. Primary deformation twins in the 2.5 Al alloy occurred in clusters like those shown in Fig. 4a and were widely separated from one another by regions containing dislocation cell structures; secondary deformation twinning, which was prevalent in the two Si alloyed steels, was scarcely observed in the 2.5 Al alloy.

Based on the TEM analysis, it is ascertained that the 2.5 Al alloy has a lower tensile work-hardening capacity than the 2.8 Si:L-Ni alloy because the 2.5 Al alloy undergoes less deformation twinning and deformation-induced martensitic transformation. It is further determined that the higher tensile work-hardening rate in the 2.5 Si alloy relative to the 2.5 Al alloy is solely the result of increased deformation twinning in the 2.5 Si alloy; the 2.5 Si alloy displays higher work hardening than the 2.5 Al alloy despite being more resistant to deformation-induced martensite than the 2.5 Al alloy (Fig. 1). Finally, it is established that the higher tensile work-hardening rate in the 2.8 Si:L-Ni alloy relative to the 2.5 Si alloy is principally a result of the lower austenite stability of the 2.8 Si:L-Ni alloy because both Si alloyed steels display similar deformation twinning behavior.

The tendency to form deformation twins increases with decreased SFE because twinning occurs via an

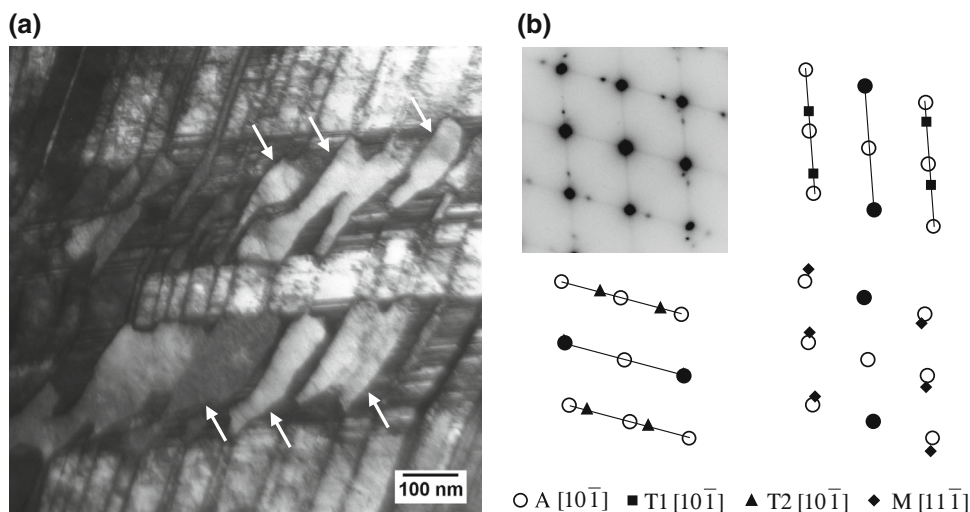


Fig. 2. (a) BF TEM micrograph of martensite nucleation (arrows) on twin intersections in the 2.5 Si alloy at 0.48 true tensile strain. (b) SADP and corresponding schematic of the martensite (M) and two deformation twin (T1 and T2) zone axis diffraction patterns relative to the parent austenite (A) diffraction pattern. The filled circles indicate overlapping austenite and twin or martensite diffraction spots. The diffraction streaking from the thin deformation twins is also indicated in the schematic SADPs.

extension of partial dislocations on adjacent austenite  $\{111\}$  planes; a lower SFE corresponds to a lower breakaway force between partial dislocations.<sup>14,15</sup> Therefore, the tensile results indicate that the Si addition to the 2.5 Si and 2.8 Si:L-Ni alloys lowers the SFE and promotes twinning, whereas the Al addition to the 2.5 Al alloy increases the SFE and inhibits twinning, which is in agreement with literature observations regarding the influences of Si and Al on the SFE.<sup>16–19</sup> The experimental measurements of SFE in the 2.5 Si and 2.5 Al alloys<sup>9</sup> corroborate this hypothesis.

The tensile tests highlight some interesting results with regard to the influence of the presence of martensite nucleation sites and the thermodynamics of austenite-to-martensite phase transformation on austenite stability during tensile loading. Si additions serve to thermodynamically stabilize austenite relative to  $\alpha'$ -martensite, and Al serves to destabilize austenite thermodynamically, based on their effects on the martensite start temperature.<sup>20,21</sup> The smaller amount of Ni in the 2.8 Si:L-Ni alloy also destabilizes austenite. Thus, even though both the 2.8 Si:L-Ni and 2.5 Al alloys have alloying additions that destabilize austenite, the austenite in the 2.8 Si:L-Ni alloy is expected to be less stable than the 2.5 Al alloy because strain-induced nucleation sites are easily generated in the 2.8 Si:L-Ni alloy because of its lower SFE. The 2.5 Si alloy is presumed to be more stable than the 2.5 Al alloy because of an increase in thermodynamic stability even though the 2.5 Si alloy has a larger propensity to generate martensite nucleation sites as a result of its lower SFE. The 2.5 Si and 2.8 Si:L-Ni alloys both display pronounced primary and secondary twinning and the generation of twin intersections, which serve as martensite nucleation

sites (Fig. 2a). However, the 2.5 Si alloy is more stable relative to the 2.8 Si:L-Ni alloy because it has a higher Ni content and therefore less thermodynamic driving force for the austenite-to-martensite phase transformation. The twin intersections in the 2.5 Si alloy infrequently nucleate martensite, and when martensite does nucleate, it only forms small particles on the order of 200 nm (Fig. 2a). However, the 2.8 Si:L-Ni alloy forms martensite bands greater than 1,000 nm long (Fig. 3a). In this view, the 2.8 Si:L-Ni alloy is both capable of forming martensite nucleation sites and is sufficiently thermodynamically unstable to generate substantial fractions of martensite on those nucleation sites. Conversely, the 2.5 Al alloy has a reduced tendency to generate martensite nucleation sites because of its higher SFE, but it has a higher capacity to form martensite relative to the 2.5 Si alloy because of the decreased thermodynamic stability associated with the higher Al and lower Si content in the 2.5 Al alloy. It should be pointed out also that for the experimental steels, deformation twin intersections are not a strict prerequisite for martensite formation; Fig. 4 shows an example of martensite formation in conjunction with primary deformation twins for the 2.5 Al alloy.

### Fatigue Deformation Behavior

Figure 5a–c show the evolution of stress amplitude and magnetic fraction with cycle number for LCF tests of the 2.8 Si:L-Ni, 2.5 Al, and 2.5 Si alloys, respectively. All three alloys exhibit an initial increase in stress amplitude with cycle number during primary cyclic hardening, followed by a plateau or even a slight decrease in stress amplitude in a region termed cyclic stabilization. Finally, near the end of the fatigue life, there is a slight

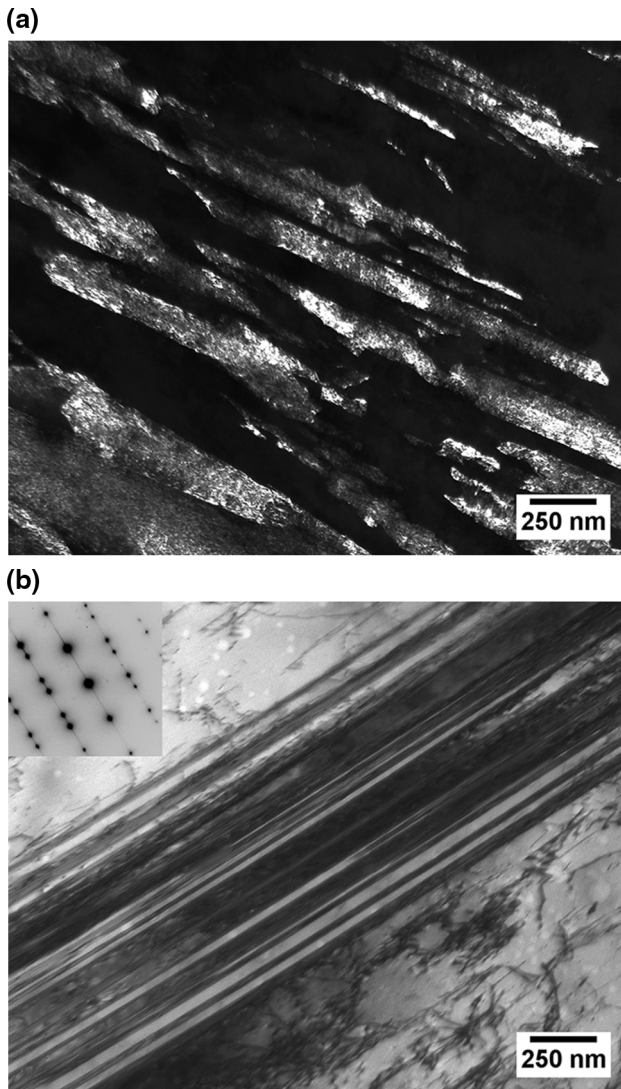


Fig. 3. (a) Martensite  $\{110\}$  DF TEM micrograph of the 2.8 Si:L-Ni alloy at 0.5 true tensile strain. (b) BF TEM micrograph of deformation twins in the 2.8 Si:L-Ni alloy at 0.14 true tensile strain and corresponding  $[011]$  austenite and twin SADP.

increase in stress amplitude for the 2.5 Si alloy and a pronounced increase in stress amplitude for the 2.5 Al and 2.8 Si:L-Ni alloys; this region is termed as secondary cyclic hardening. The drop in stress amplitude at the end of the fatigue life is the result of macroscopic fatigue crack propagation.

The magnetic fractions from specimens interrupted at specific cycle numbers are also shown in Fig. 5a–c. Minimal deformation-induced martensite is formed in any of the alloys during primary cyclic hardening. Appreciable fractions of martensite are not formed in the 2.5 Al and 2.8 Si:L-Ni alloys until after the material has experienced a finite lifetime, approximately 100 cycles, in the cyclic stabilization regime. The generation of martensite at this point leads to the pronounced secondary cyclic hardening displayed in these two alloys. Because the stress

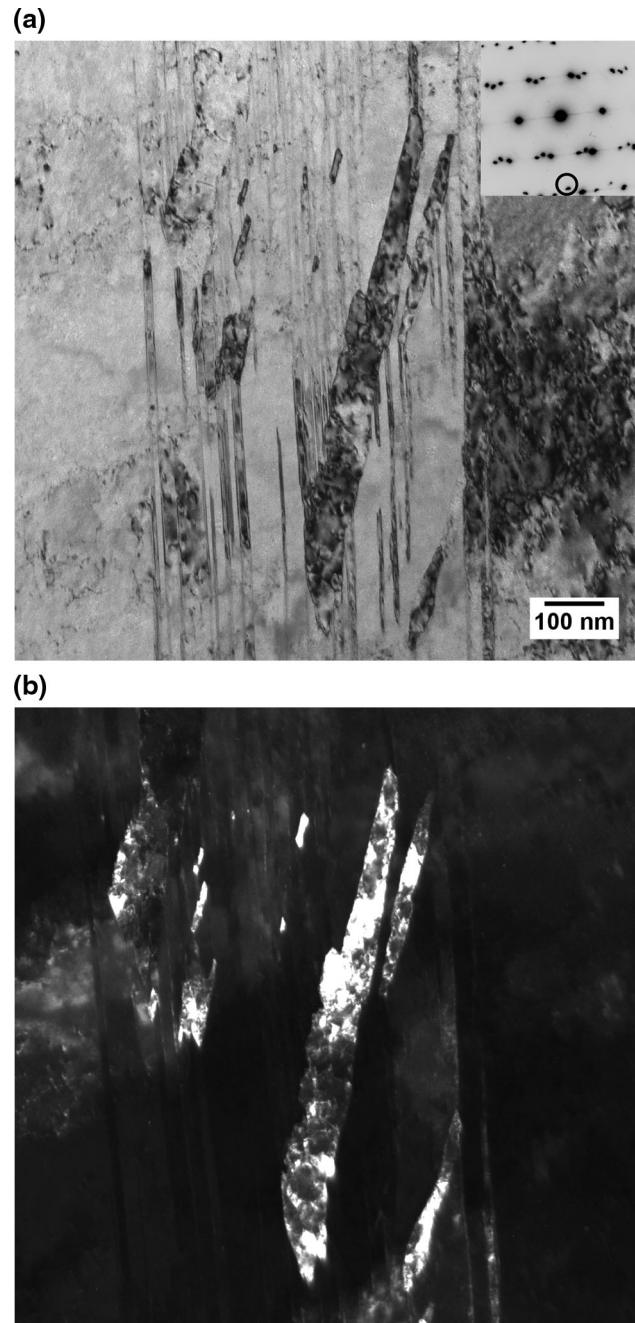


Fig. 4. (a) BF TEM micrograph of deformation twins and martensite in the 2.5 Al alloy at 0.37 true tensile strain. (b) Martensite  $(211)$  DF TEM image [diffraction spot circled in (a)]. The electron beam orientation is similar to that shown in Fig. 2b but without the presence of a second twin (T2) orientation.

amplitude is constant or even slightly decreases during the cyclic stabilization regime that precedes martensite formation, it can be ascertained that the martensite is initiated via strain-induced nucleation; stress-assisted nucleation occurs as increases in applied stress supply an additional driving force for transformation.<sup>22,23</sup> Of course, the increases in stress amplitude that accompany martensite formation

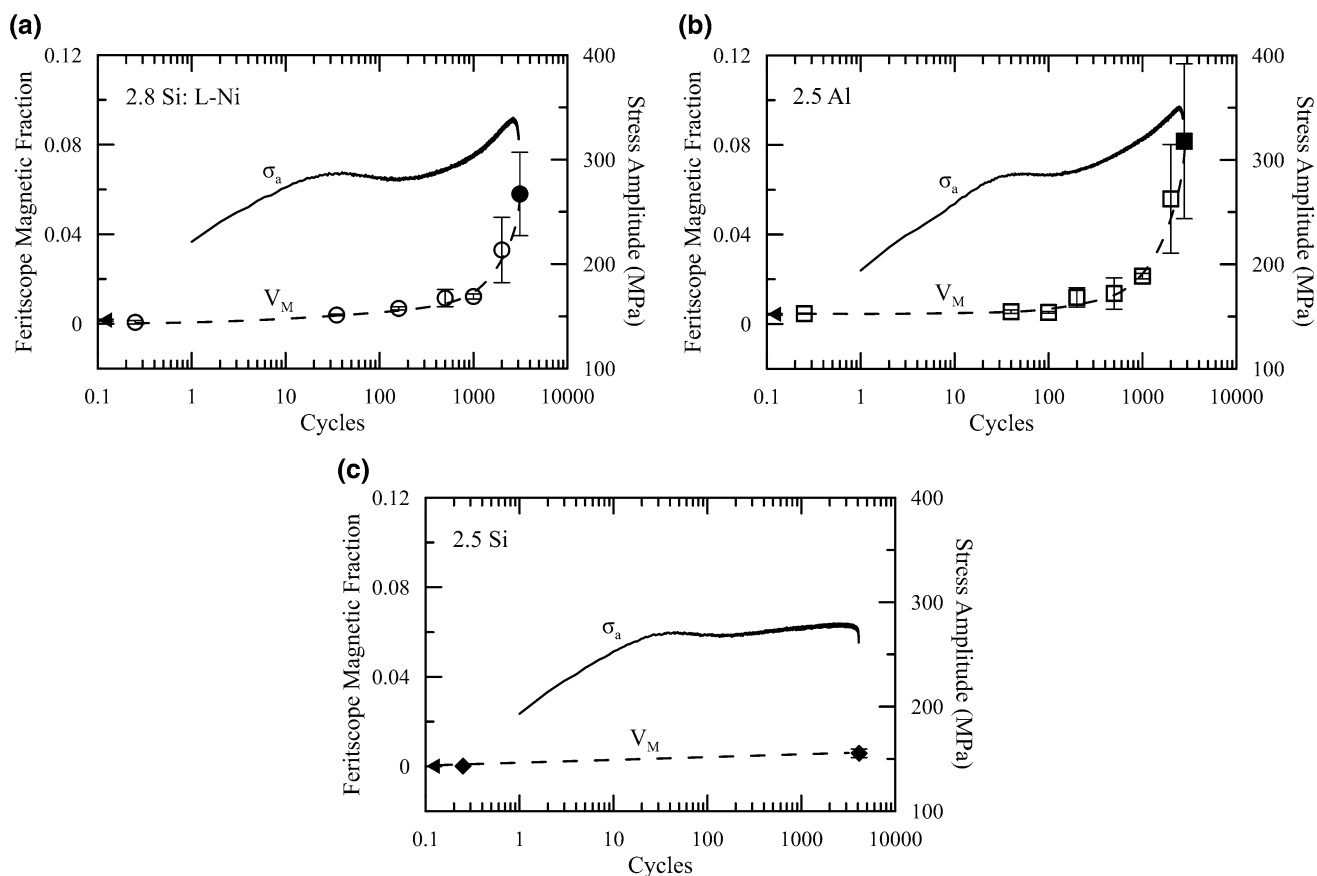


Fig. 5. Evolution of stress amplitude ( $\sigma_a$ ) and magnetic fraction ( $V_M$ ) with cycle number for the (a) 2.8 Si:L-Ni, (b) 2.5 Al, and (c) 2.5 Si alloys fatigue tested at a total strain amplitude of 0.6%. Closed  $V_M$  symbols correspond to the sample cycled to failure; open symbols correspond to interrupted tests. The filled triangles indicate the  $V_M$  at zero cycles (annealed condition).

cannot be ruled out from contributing a stress-assisted component to subsequent martensite formation. Furthermore, the formation of martensite at the end of the cyclic stabilization regime implies that a specific deformation substructure, which results from cyclic plasticity, is necessary for martensite formation during fatigue loading. The 2.5 Si alloy is very stable against martensite formation throughout its fatigue life, and therefore, it experiences minimal secondary cyclic strain hardening.

The amount of martensite transformation during fatigue is comparable in the 2.5 Al and 2.8 Si:L-Ni alloys despite the differences in deformation and transformation behavior observed in tension. Also, the amount of martensite formed at 0.6% total strain amplitude is greater than the amount formed at a monotonic tensile strain of 0.6% for both alloys. Therefore, strain-induced martensite transformation during cyclic plastic deformation cannot be directly correlated to transformation during monotonic plastic deformation. The evolution of deformation substructure and associated strain-induced martensite transformation during fatigue loading

was characterized using TEM and compared to the observations made for tensile deformation.

Primary cyclic strain hardening occurs through the generation and interaction of dislocations in the initially annealed structure.<sup>24,25</sup> Cyclic stabilization occurs through the formation of dislocation structures originating from localized plastic strain.<sup>24,25</sup> Li and Laird<sup>26</sup> fatigue loaded AISI 316L stainless steel in the cyclically stabilized regime and observed slip planes containing a high density of parallel dislocations that were partially dissociated, resulting in irregular stacking fault contrast on the slip bands. The AISI 316L steel was stable against martensitic transformation in the experimental conditions that were used. Figure 6a shows martensite formation associated with similar types of slip bands (arrows) in the 2.8 Si:L-Ni alloy cycled to failure at 0.6% total strain amplitude. The DF TEM micrograph in Fig. 6b highlights the martensite. Because Li and Laird<sup>26</sup> observed these dislocation structures without martensite formation, it can be surmised that the slip bands in Fig. 6a are not a consequence of the martensitic transformation. Furthermore, slip bands like those in Fig. 6a are

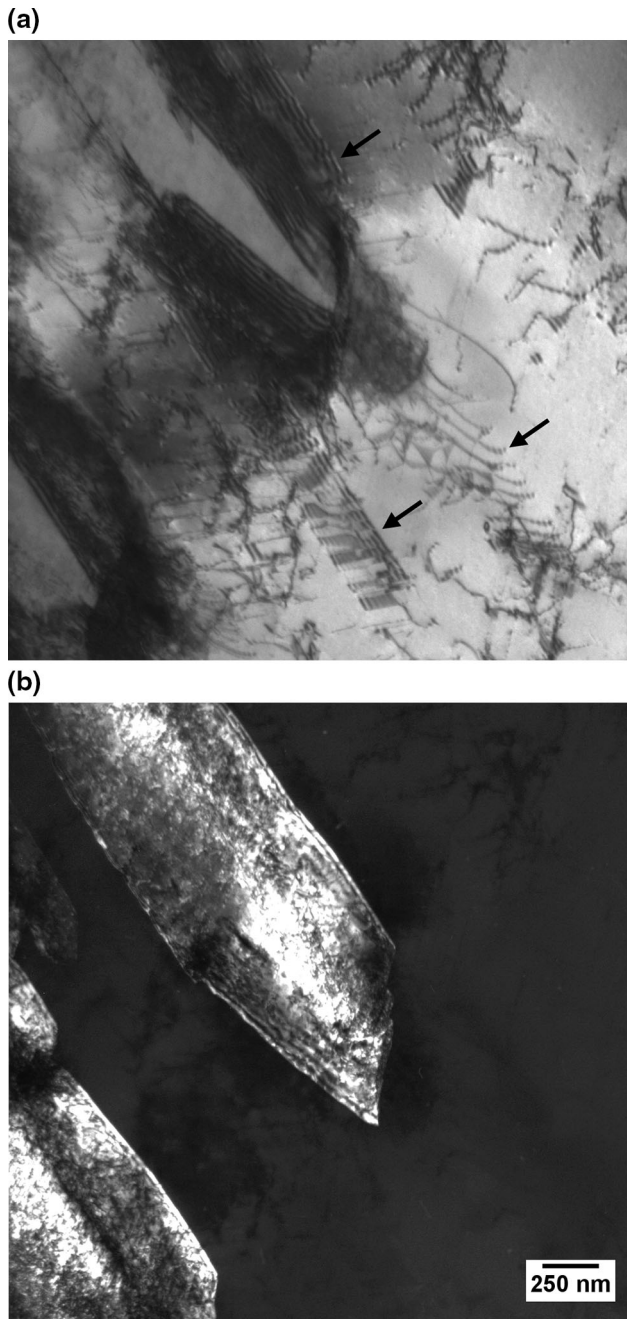


Fig. 6. (a) BF TEM micrograph of martensite adjacent to austenite slip bands (arrows) containing dissociated dislocations in the 2.8 Si:L-Ni alloy cycled to failure ( $N_F = 3,114$ ) at 0.6% total strain amplitude. The electron beam is near [011] austenite and the arrows in the image are parallel to [200] austenite. Fringe contrast indicates that the shear bands and austenite/martensite interfaces are inclined to the electron beam. (b) Martensite {110} DF TEM micrograph.

expected to precede martensite formation because martensite nucleation occurs after a finite lifetime in the cyclic stabilization regime during which the slip bands form, according to the observations made by Li and Laird.<sup>26</sup>

Specimens of the 2.5 Al alloy were interrupted after 500 cycles (early stage of secondary hardening)

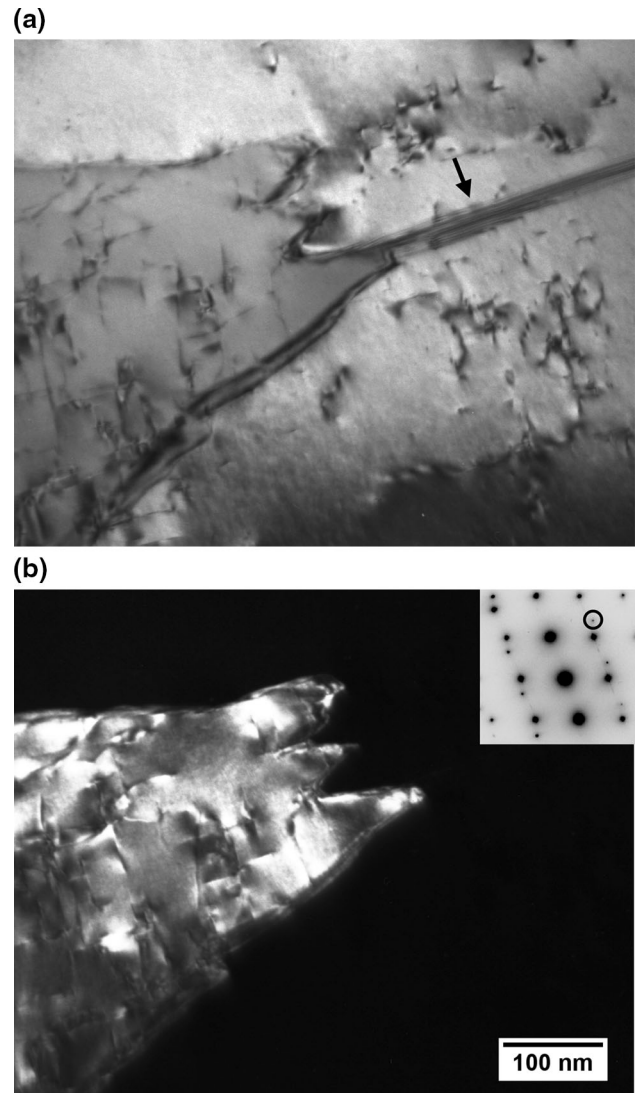


Fig. 7. (a) BF TEM micrograph of martensite adjacent to extended stacking faults (arrow) in the 2.5 Al alloy cycled  $N = 500$  times at 0.6% total strain amplitude. (b) Martensite (020) DF TEM micrograph. The electron beam is near [011] for austenite and [001] for martensite.

at 0.6% total strain amplitude for TEM evaluation to further characterize the deformation substructures that precede martensite formation. Figure 7a and b shows martensite formation adjacent to extended stacking faults in the 2.5 Al alloy after 500 cycles, which indicates that extended stacking faults may also serve as plastic strain localization sites that precede martensite formation during fatigue loading. Bands of hexagonal close-packed  $\epsilon$ -martensite have also been observed to nucleate  $\alpha'$ -martensite during fatigue loading of metastable austenitic steels.<sup>3-7</sup>

These TEM observations show that regions of plastic strain localization, such as concentrated bands of dislocations, extended stacking faults, and  $\epsilon$ -martensite, are sites of  $\alpha'$ -martensite formation during LCF loading. All the sites identified for

$\alpha'$ -martensite formation during LCF would, upon first consideration, be more readily formed in a material with a lower SFE than a higher SFE. The 2.8 Si:L-Ni alloy would therefore be expected to undergo more martensitic transformation than the 2.5 Al alloy during fatigue loading. However, in their fatigue analysis of AISI 316L, Li and Laird pointed out that slip bands like those shown in Fig. 6a for the 2.8 Si:L-Ni alloy form only in alloys with an intermediate SFE, not low-SFE materials like Cu-16Al (SFE  $\sim 3$  mJ/m<sup>2</sup>) or higher SFE materials like Cu (SFE  $\sim 50$  mJ/m<sup>2</sup>). They argued that whereas a low SFE facilitates the confinement of slip to discrete bands, it may also inhibit the nucleation of new shear bands through dislocation cross slip from saturated shear bands. Therefore, shear band formation may actually be promoted by intermediate SFEs and depend only weakly on SFE over a certain range.

It is established that Si reduces the austenite stacking fault energy, and the observations of deformation substructure in tension confirm this finding. The lower SFE of the 2.8 Si:L-Ni alloy allows it to twin in tension, and the intersection of these twins facilitates the nucleation of martensite. However, during fatigue loading, deformation twins do not readily form in any of the experimental alloys. The deformation substructures that develop during fatigue of the 2.8 Si:L-Ni and 2.5 Al alloys both contain planar deformation features that nucleate  $\alpha'$ -martensite. The 2.5 Al and 2.8 Si:L-Ni alloys must have comparable thermodynamic austenite stabilities because the fatigue-induced nucleation sites yield comparable martensite fractions in the two alloys. In contrast, whereas the 2.5 Si alloy also forms some deformation structures similar to those formed in the 2.5 Al and 2.8 Si:L-Ni alloys, it is resistant to transformation in tension and fatigue and must have higher thermodynamic austenite stability than the other two alloys.

The tension and fatigue results of the 2.5 Al and 2.8 Si:L-Ni alloys indicate that austenite stability during fatigue loading does not necessarily correlate to austenite stability during tensile loading. This can be attributed to differences in strain-induced martensite nucleation between the two loading conditions. During tensile loading, martensite nucleation occurs on deformation twins and their intersections. During fatigue loading, martensite nucleation occurs instead in regions of plastic strain localization that develop in the cyclic stabilization regime of the fatigue life. A possible explanation for the lack of deformation twinning during LCF is that the stresses achieved during fatigue loading do not exceed the partial dislocation breakaway stress that must be overcome to initiate deformation twinning. The plateau in the tensile work-hardening curve of the 2.8 Si:L-Ni alloy (Fig. 1a), which has been correlated to the onset of deformation twinning,<sup>27</sup> occurs near a true strain of 0.1 and a true stress of 400 MPa. During LCF loading at 0.6% total strain

amplitude, the maximum stress amplitude achieved by any of the alloys is 340 MPa, and thus the stress might not be sufficient to initiate deformation twinning at this strain amplitude. It should be pointed out that deformation twins have been observed, in AISI 316L stainless steel for example, after LCF loading at sufficiently high plastic strain amplitudes.<sup>28</sup>

## SUMMARY AND CONCLUSIONS

Three experimental alloys were produced with different stacking fault energies and austenite stabilities, primarily through silicon, aluminum, and nickel additions. Stacking fault energy strongly affected deformation mechanisms in tension; the alloys with silicon additions exhibited significant deformation twinning because of their low stacking fault energy, whereas the alloy with aluminum additions deformed mostly through dislocation slip. Twin intersections served as nucleation sites for  $\alpha'$ -martensite and especially promoted martensite formation in the 2.8 Si:L-Ni alloy, which also likely had relatively low thermodynamic austenite stability as a result of the low Ni content. However, the stacking fault energy did not strongly affect deformation mechanisms in fatigue. Martensite formed in regions of localized plastic deformation regardless of the alloy stacking fault energy. The amount of martensite that formed during fatigue loading was comparable in the 2.8 Si:L-Ni alloy and 2.5 Al alloy, implying that the alloys had similar thermodynamic austenite stability. The thermodynamic driving force for strain-induced martensite transformation was lowest in the 2.5 Si alloy, as it formed minimal amounts of martensite in tension or fatigue, despite forming both tensile and fatigue deformation features that nucleated martensite in the other two alloys. The results suggest that the role of stacking fault energy on austenite stability may be more influential in tension than fatigue loading, particularly when the stacking fault energy is such that twinning promotes strain-induced martensite nucleation in tension. If the stress is not sufficient for twinning deformation to occur in fatigue, then thermodynamic stability of austenite may be more important than stacking fault energy for alloys that develop similar deformation substructures.

## ACKNOWLEDGEMENT

The support of the Advanced Steel Processing and Products Research Center (ASPPRC), the National Science Foundation CAREER Award No. 0955236, and the U.S. Department of Energy Office of Science Graduate Fellowship Award are gratefully acknowledged. Prof. Bruno De Cooman, Professor and Director of the Materials Design Laboratory GIFT, POSTECH, is also acknowledged for his help with transmission electron microscopy.



## REFERENCES

1. G.B. Olson and M. Cohen, *Metall. Trans. A* 6, 791 (1975).
2. L. Bracke, L. Kestens, and J. Penning, *Scripta Mater.* 57, 385 (2007).
3. D. Hennessy, G. Steckel, and C. Altstetter, *Metall. Trans. A* 7, 415 (1976).
4. J.-B. Vogt, J. Foct, C. Regnard, G. Robert, and J. Dhers, *Metall. Trans. A* 22, 2385 (1991).
5. A. Weidner, A. Glage, and H. Biermann, *Procedia Eng.* 2, 1961 (2010).
6. A. Glage, A. Weidner, and H. Biermann, *Procedia Eng.* 2, 2085 (2010).
7. A. Das, S. Sivaprasad, P.C. Chakraborti, and S. Tarafder, *Mater. Sci. Eng. A* 528, 7909 (2011).
8. M.L. Glenn, *J. Mater. Eng.* 10, 181 (1988).
9. G.R. Lehnhoff (Ph.D. Dissertation, Colorado School of Mines, 2013).
10. ASTM E606-04, *Standard Practice for Strain-Controlled Fatigue Testing* (Philadelphia: ASTM, 2004).
11. J. Talonen, P. Aspegren, and H. Hanninen, *Mater. Sci. Technol.* 20, 1506 (2004).
12. M. Loretto and R. Smallman, *Defect Analysis in Electron Microscopy* (London: Chapman and Hall, 1975), p. 2.
13. D. Williams and C. Carter, *Transmission Electron Microscopy*, 2nd ed. (New York: Springer, 2009), p. 167.
14. T.S. Byun, *Acta Mater.* 51, 3063 (2003).
15. K.-T. Park, G. Kim, S.K. Kim, S.W. Lee, S.W. Hwang, and C.S. Lee, *Metall. Mater. Int.* 16, 1 (2010).
16. R.E. Schramm and R.P. Reed, *Metall. Trans. A* 6, 1345 (1975).
17. C.G. Rhodes and A.W. Thompson, *Metall. Trans. A* 8, 1901 (1977).
18. A. Dumay, J.-P. Chateau, S. Allain, S. Migot, and O. Bouaziz, *Mater. Sci. Eng. A* 483–484, 184 (2008).
19. J. Kim, S.-J. Lee, and B.C. De Cooman, *Scripta Mater.* 65, 363 (2011).
20. C.Y. Kung and J.J. Rayment, *Metall. Trans. A* 13, 328 (1982).
21. K. Ishida, *J. Alloys Compd.* 220, 126 (1995).
22. G.B. Olson and M. Cohen, *J. Less-Common Met.* 28, 107 (1972).
23. P.C. Maxwell, A. Goldberg, and J.C. Shyne, *Metall. Trans.* 5, 1305 (1974).
24. M. Klesnil and P. Lukas, *Fatigue of Metallic Materials*, 2nd ed. (New York: Elsevier, 1992), p. 35.
25. H.-J. Christ, *ASM Handbook Vol. 19 Fatigue and Fracture* (Materials Park: ASM International, 1996), p. 73.
26. Y. Li and C. Laird, *Mater. Sci. Eng. A* 186, 87 (1994).
27. E. El-Danaf, S.R. Kalidindi, and R.D. Doherty, *Metall. Mater. Trans. A* 30, 1223 (1999).
28. M. Gerland, J. Mendez, P. Violan, and B.A. Saadi, *Mater. Sci. Eng. A* 118, 83 (1989).